Volume 9
Number 42
14 November 2021
Pages 14949–15382

# Journal of Materials Chemistry C

Materials for optical, magnetic and electronic devices

rsc.li/materials-c

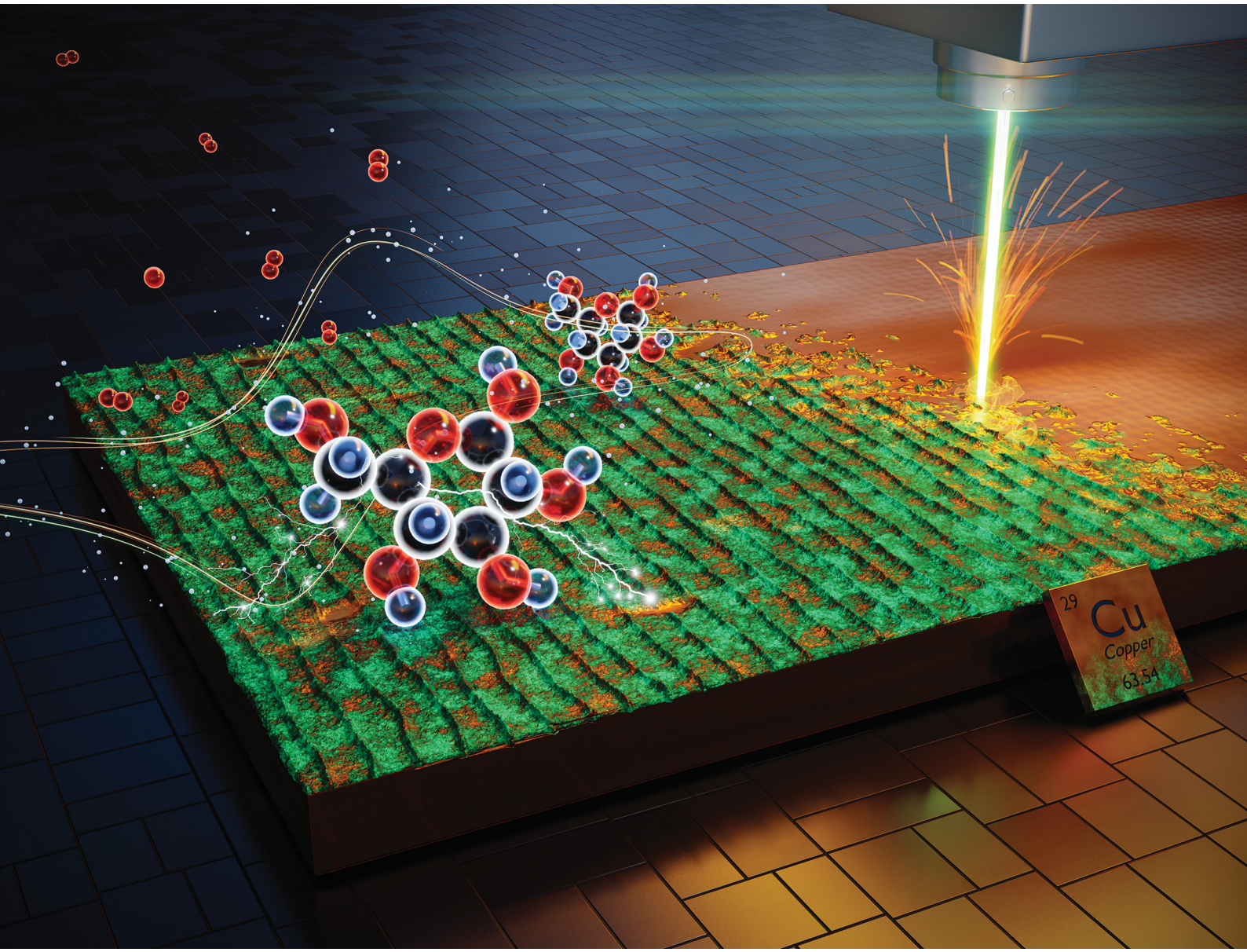


ISSN 2050-7526

ROYAL SOCIETY OF CHEMISTRY

**PAPER**

Rahim Rahimi *et al.*

Laser-induced atmospheric $Cu_xO$ formation on copper surface with enhanced electrochemical performance for non-enzymatic glucose sensing

Journal of Materials Chemistry C

ROYAL SOCIETY OF CHEMISTRY

PAPER

View Article Online
View Journal | View Issue



Cite this: J. Mater. Chem. C, 2021, 9, 14997

# Laser-induced atmospheric $Cu_xO$ formation on copper surface with enhanced electrochemical performance for non-enzymatic glucose sensing†

Sotoudeh Sedaghat,[ab] Sina Nejati,[ab] Luis Helena Bermejo,[ab] Zihao He,[c] Alejandro M. Alcaraz,[a] Alexander Roth,[ad] Zheng Li,[e] Vilas G. Pol,[e] Haiyan Wang[abc] and Rahim Rahimi*[ab]

Copper oxide nanostructures are widely used for various applications due to their unique optical and electrical properties. In this work, we demonstrate an atmospheric laser-induced oxidation technique for the fabrication of highly electrochemically active copper oxide hierarchical micro/nano structures on copper surfaces to achieve highly sensitive non-enzymatic glucose sensing performance. The effect of laser processing power on the composition, crystallinity, microstructure, wettability, and color of the laser-induced oxide on copper (LIO-Cu) surface was systematically studied using scanning electron microscopy (SEM), grazing incidence X-ray diffraction (GI-XRD), Raman spectroscopy, energy dispersive X-ray spectroscopy (EDX), EDX-mapping, water contact angle measurements, and optical microscopy. Results of these investigations showed a remarkable increase in copper oxide composition by increasing the laser processing power. The pore size distribution and surface area of the pristine and LIO-Cu sample estimated by $N_2$ adsorption–desorption data showed a developed mesoporous LIO-Cu structure. The size of the generated nano-oxides, crystallinity, and electroactivity of the LIO-Cu were observed to be adjustable by the laser processing power. The electrocatalytic activity of LIO-Cu surfaces was studied by means of cyclic voltammetry (CV) within a potential window of −0.8 to +0.8 V and chronoamperometry in an applied optimized potential of +0.6 V, in 0.1 M NaOH solution and phosphate buffer solution (PBS), respectively. LIO-Cu surfaces with optimized laser processing powers exhibited a sensitivity of 6950 μA $mM^{-1}$ $cm^{-2}$ within a wide linear range from 0.01 to 5 mM, with exceptional specificity and response time (<3 seconds). The sensors also showed excellent response stability over a course of 50 days that was originated from the binder-free robust electroactive film fabricated directly onto the copper surface. The demonstrated one-step LIO processing onto commercial metal films, can potentially be applied for tuneable and scalable roll-to-roll fabrication of a wide range of high surface area metal oxide micro/nano structures for non-enzymatic biosensing and electrochemical applications.

Received 19th March 2021,
Accepted 23rd June 2021

DOI: 10.1039/d1tc01289d

rsc.li/materials-c



## Introduction

Copper oxide compounds ($Cu_xO$) including cupric oxide (CuO) and cuprous oxide ($Cu_2O$) are the most common forms of the copper oxides with unique optical and electrical properties.[1–5] Owing to these features, $Cu_xO$ structures have been used for a wide range of applications including electrochemical sensing,[6–10] gas detection,[11–13] photovoltaic energy conversion,[14,15] biofouling prevention,[16,17] and photochemical catalysis.[18–21] In addition to chemical composition, their distinctive crystallographic feature and shape are also two important key factors that determine the overall physical and chemical properties of many types of $Cu_xO$ structures.[22,23] Although high-index facets containing a high density of low-coordinated atoms (including edges, steps, and kinks) offer highly active sites for catalysis and sensing

[a] Birck Nanotechnology Center, Purdue University, West Lafayette, IN, 47907, USA. E-mail: rrahimi@purdue.edu
[b] School of Materials Engineering, Purdue University, West Lafayette, IN, 47907, USA
[c] School of Electrical and Computer Engineering, Purdue University, West Lafayette, IN, 47907, USA
[d] School of Mechanical Engineering, Purdue University, West Lafayette, IN, 47907, USA
[e] Davidson School of Chemical Engineering, Purdue University, West Lafayette, IN, 47907, USA

† Electronic supplementary information (ESI) available. See DOI: 10.1039/d1tc01289d

applications, these facets are highly unstable and challenging to be prepared by traditional chemical synthesis and deposition techniques.[22,24–26] Therefore, the primary approach to enhance catalytic activity of $Cu_xO$ structures with stable performance is to increase their effective surface area by synthesizing them in the form of micro/nano structures in low-index crystalline (*i.e.*, the (111), (110), and (100) facets) or amorphous phases.[27–29] Over the past few decades, various routes for the synthesis of such unique $Cu_xO$ nanostructures have been investigated for different applications such as thermal oxidation, electrodeposition processes,[30] soft template approaches,[31] radiolytic reduction,[32] chemical vapor deposition,[33] and solvothermal and chemical reduction.[34] However, many of such methods often involve use of complex processes with environmentally unfriendly chemicals and long processing time.[35,36]

Recently, laser-assisted processing technologies have been demonstrated as an alternative to overcome many challenges associated with conventional chemical processing technologies with a wide range of advantages as a scalable, rapid, green, and tunable fabrication technique in ambient conditions.[37–39] They have been employed for a wide range of scalable manufacturing technologies including deposition, carbonization,[40] surface functionalization,[41] oxidation,[37] and texturing[42,43] of different surfaces for a variety of applications. Many nanocrystalline $Cu_xO$ compounds synthesized through laser-assisted processing technologies have been focused on the use of laser ablation of a solid target in a confining liquid. This technique consists of an interaction of a high-power laser beam with a solid target that is immersed in a liquid solution. The confining liquid provides a media where the chemical interaction of the laser beam with the surrounding takes place and the generated micro/nano particles are collected simultaneously. It has been found that by simply changing the confining liquid and laser settings, interesting chemical reactions can take place at the interface between the laser ablated region and the liquid, allowing the synthesis of different $Cu_xO$ compounds with unique micro/nano structures. For instance, Jung *et al.*[44] investigated the synthesized Cu-based nanoparticles by pulsed Nd:YAG laser ablation in different concentrations of NaOH as the confining liquid where they found that mostly spherical shape $Cu_2O$ nanoparticles with an average diameter of about 20 nm were formed at lower NaOH concentrations, whereas CuO leaf-shaped nanorods of 100 nm in length was created at higher NaOH concentrations. Although liquid-based laser processing techniques have shown to provide an excellent route for scalable synthesis of $Cu_xO$ nanostructures, their products are in colloidal suspension forms which will often require additional complex steps to properly immobilize them onto a conductive electrode surfaces as a functional coating for catalytic and biosensing applications. Therefore, using more straightforward laser-assisted procedures to directly synthesize functional $Cu_xO$ nanostructures onto a copper surface in atmospheric conditions not only can significantly reduce the process complications, but also provides a more stable and robust electrical interface between the copper oxide nanoparticles and the underlying copper electrode, called laser-induced oxidation (LIO).[37] It is well known that laser beams can be used to oxidize metallic surfaces with well-defined micro and nano structure through a localized thermal oxidation that occurs due to the chemical reaction between the metal and oxygen molecules present in the atmosphere.[45,46] Applying LIO onto Cu metal surfaces with controlled laser beams have also been associated with the formation of robust porous metal oxide nanostructures of cuprous oxide ($Cu_2O$) or cupric oxide (CuO).[47] Despite the great potential and simplicity of such LIO technologies in creating unique $Cu_xO$ compounds with controllable micro/nano structures on Cu metal surface, their applications are limited to enhancing optical properties,[48] antibacterial performance,[38] and corrosion resistance of Cu surfaces.[47] For instance, Tang *et al.*[48] reported using nanosecond pulsed laser blackening of copper in ambient conditions which resulted in an organized structure with over 97% light absorbance. In another study, Selvamani[38] *et al.* observed the enhanced bactericidal properties of atmospheric laser textured copper surfaces through selective modification of surface topography and chemistry. Also, Boinovich *et al.*[47] reported employing controlled atmosphere laser texturing followed by a chemisorption of low energy compound to fabricate copper oxide structure to use as a durable coating. Their technique resulted in a triple layer superhydrophobic laser-induced copper oxide surface with high superhydrophobic properties. Nevertheless, among studies the effect of laser processing conditions such as laser power on the obtained $Cu_xO$ composition, microstructure, and electrochemical sensing, and the correlation between those generated structures with electrochemical performance, have not been systematically studied to date. Moreover, the technique of direct LIO onto the Cu surface for its application in biosensing has not previously been demonstrated.

In this work, we demonstrate one-step fabrication of electroactive hierarchical copper oxide with micro/nano structure directly onto a copper surface by LIO in ambient conditions. Type and quantity of the copper oxide species, feature size, porosity, wettability, and morphology of the LIO-Cu film and its effect on electrochemical activity were studied using different laser processing power settings which eventually nominates it as a promising candidate to be employed in non-enzymatic glucose sensing applications. Moreover, a comparison of sensitivity, selectivity, reproducibility, and long-term stability of LIO-Cu surfaces with optimized electrocatalytic activity against other state-of-the-art non-enzymatic glucose sensors based on a Cu-nanoparticle-modified surfaces is provided to demonstrate the superior performance as well as economic advantage against other technologies. Finally, this study provides systematic investigation of the laser processing power conditions, not only for optimized electrocatalytic activity, but also for the surface morphology of the processed material which will determine the required minimum copper substrate thickness for each processing condition.

## Experimental details

### Laser-induced copper oxide

One-step fabrication of copper oxide film was performed by applying a nanosecond pulsed ND:YAG laser beam (Universal

 

Laser Systems Inc., Scottsdale, AZ, USA) with a wavelength of 1.06 μm onto commercial 99.9% copper metal foil (Yodaoke inc. Nanjing Baoyijia Trading Co., China) with thickness of 0.05 mm. The laser system was operated at different laser powers of 16, 20, 24, 28, 32, 36, and 40 W with a scanning speed of 4 m $s^{-1}$. The laser beam profile followed a Gaussian distribution with a spot size of 63 μm and repetition frequency of 30 kHz, resulting in a 28.3 μm overlap with an overlapping rate of ~45%. The LIO-Cu samples were labeled as *x*LIO-Cu (from 16LIO-Cu to 40LIO-Cu) in which *x* represents the applied laser power.

### Electrode preparation

All electrodes were passivated by silicon glue (80 050 clear RTV silicone adhesive sealant, Permatex Inc., Solon, OH, USA, with temperature stability range of −59 °C to 204 °C), leaving a 2 × 2 $mm^2$ opening as an electroactive area at one end and an opening for electrical connection at the other end (Fig. S1, ESI†). This passivation is required for the restriction of the electrode activity to the opening area and to prevent any possible unwanted side reaction of interconnection part of the electrode with the solution. The prepared electrodes were collected for electrochemical tests without further treatments.

### Surface characterization

Optical microscopy (MicroZoom high performance microscope, Bausch & Lomb, Rochester, NI, USA) and scanning electron microscopy (SEM, Dual-Beam Helios SEM, ThermoScientific, Hillsboro, OR, USA) images were used to characterize the color change and superficial morphology of the Cu surface before and after LIO process at different laser power settings. Chemical compositions and elemental distribution throughout the samples were assessed using the FE-SEM field emission SEM (FE-SEM, Hitachi-S 4800, Tokyo, Japan) equipped with an EDX detector (Oxford Instruments, Abington, UK). Further SEM images with the sample tilted 87° and rotated 5° were taken to show the surface profile. Crystallographic features of the *x*LIO-Cu samples were analyzed using grazing incident X-ray diffraction (GI-XRD) with a fixed Cu Kα anode ($\lambda$ = 1.541, 87 Å) operating at 45 kV and 40 mA with an incident beam angle fixed at $\omega$ = 3° which was optimized by analysis of the XRD of the samples within different beam incident angles (PANalytical, Almelo, The etherlands). Briefly, a range of X-ray incident beam angles from 0.5–3° were explored for GI-XRD analysis and compared with each other as well as the regular beam angle XRD data in Fig. S2 (ESI†). Since, the $\omega$ = 3° data represented the highest peak intensity for $Cu_2O$ phase, indicating the best beam incident angle, we collected all XRD results based on this specific incident angle. Raman spectra of the samples were recorded using a Raman spectrometer (Ranishaw Invia, IL, USA) equipped with a 532 nm laser. The size distribution of the LIO-Cu surfaces was evaluated by SEM image processing using ImageJ software bundled with Java 1.8.0. Attenuated total reflection Fourier-transform infrared spectroscopy (ATR-FTIR) spectra for pristine and LIO-Cu samples were collected using a PerkinElmer spectrum 100 FTIR spectrometer (Waltham, MA, USA). For thickness and roughness analysis, profile contact scans using a profilometer (P-7 Tencor, KLA, Milpitas, CA) were performed for pristine and LIO-Cu samples fabricated with different laser power. The scans were performed through a length of 5 mm, with a scan speed of 20 μm $s^{-1}$, and a sampling rate of 500 Hz, using a stylus force of 1 mg, and a range/resolution of 13 μm/8 nm. Wettability properties of the samples were quantified using static water contact angle measurement with 5 μL droplet of deionized water (Advanced Goniometer 290f, ramé-hart Instrument Co. Succasunna, NJ, USA). $N_2$ adsorption–desorption data was obtained using a Quantachrome NOVA station: A (Boynton Beach, FL, USA), running with NovaWin software (version 11.0). To measure the specific surface area and pore size distribution of the pristine and LIO-Cu samples, about 2 g of the samples were chopped into small pieces (2 × 2 $mm^2$). First the samples were degassed at 200 °C for 24 hours under 10 psi and then nitrogen adsorption was performed at 0 K.

### Electrochemical characterization

Electrochemical measurements were carried out using a Gamry system (Reference 3000 Potentiostat/Galvanostat/ZRA, Gamry Instruments, PA, USA) controlled by a data acquisition Gamry framework software (version 6.23). For all electrochemical tests, a three-electrode configuration with a pristine Cu or *x*LIO-Cu electrode with an active area of 0.04 $cm^2$ was used as working electrode, a platinum coil as a counter, and a commercial 3 M KCl, Ag/AgCl (Gamry silver/silver chloride reference electrode, Gamry Instruments, PA, USA) as a reference electrode. Cyclic voltammograms (CV) were recorded in a potential window of −0.8 to +0.8 V (*vs.* Ag/AgCl) in 0.1 M NaOH as a background electrolyte. Glucose solution was added from a 10 mM stock solution to the electrolyte when needed. To simulate the pH of the real sample, the amperometric response toward glucose was recorded in 0.1 M phosphate buffer solution (PBS) with pH 7.4.[49] Chronoamperometric profiles were recorded at applied potentials of +0.4, +0.5, +.6, and +0.7 V *versus* Ag/AgCl reference electrode with successive addition of pre-determined amounts of glucose stock solution to 10 mL of PBS electrolyte with continuous magnetic stirring under ambient conditions. The optimized potential of +0.6 V was applied for all other measurements. Recovery time and reproducibility of response, as well as reusability of the developed LIO-Cu electrodes were investigated using chronoamperometric tests at +0.6 V. Briefly, to assess the reproducibility and recovery time, the amperometric responses for the LIO-Cu electrode were recorded by cyclic response collection in the blank PBS and 250 μM glucose solution for 17 continuous cycles. In order to validate long-term stability and reusability of the LIO-Cu electrodes, the stepwise sensitivity of the LIO-Cu electrodes toward glucose (concentration range of 0.1–1 mM) was evaluated over a course of 50 days. The used electrodes were stored in ambient conditions without further cleaning after each measurement. Besides, for evaluation of the LIO-Cu structure change after glucose oxidation test, one of the electrodes was analyzed using GIXRD technique after amperometric test performed in 2 mM of

glucose. To examine the anti-interference nature of the proposed electrochemical sensor, chronoamperometric response of LIO-Cu electrode toward different interfering agents was recorded. The experiment was carried out by addition of glucose to PBS background solution, followed by stepwise addition of the potential interfering reagents including uric acid (UA), L-ascorbic acid (As), acetic acid (AA), acetaminophen (AC), glutamic acid (GA), citric acid (CA), and NaCl with equal concentrations of 100 mM. This study was finalized by further glucose addition and recording the output current change.

## Results and discussion

### Material characterization

Fig. 1a illustrates the schematic of the process for drawing of a computer-controlled pattern onto the copper surface. As it is depicted in Fig. 1b, irradiation of the copper surface by a ND:YAG laser beam under ambient condition converted the copper surface to a dark copper oxide film. By employing a computer-controlled laser scribing, LIO pattern can be readily written into the desired geometry as shown in Fig. 1b. The figure shows the patterned Purdue University train logo on the copper surface with five distinguished colours, each of which is attributed to an oxidation degree of copper displaying the effect of laser induction with specific powers. To further assess the laser power effect on the morphology and microstructure, we performed microscopic imaging and surface profilometry of copper samples that were processed at different laser power settings. Fig. 2a displays a realistic picture of an LIO copper surface that is patterned with a Purdue University logo applying laser powers ranging from 16 W to 40 W with a constant irradiation time. Generally, in visible light, $Cu_2O$ adsorbs energies higher than its gap (2.17 eV) which contains all colours but red that explains its observed colour.[50] On the other hand, CuO absorbs almost all wavelengths which explains its observed colour (black). In Fig. 2a, beginning at 16 W, copper colour changed to a dominated red colour that was attributed to the oxidation of copper to $Cu_2O$ phase. Since the temperature change on the irradiated zone depends on the applied laser energy, the colour change could be modulated by the degree of oxidation controlled with the laser power. Thus, increasing the laser power, provided enough energy for the further oxidation of $Cu_2O$ to produce CuO which appeared as a dark red (brownish) colour on the samples patterned with higher laser energy (*e.g.*, $>24$ W). As expected, increased laser power to 40 W led to a darker surface which can be explained by the increase in the ratio of CuO species with black colour. The gradual darkening of the surface as a result of increased oxidation degree is clearly shown in optical microscopic images in Fig. 2(c–i). These figures also demonstrated a developed roughness on the surface of the LIO-Cu samples because of the laser texturing phenomena. The stripped patterns on the surface of LIO-Cu samples were caused by laser scribing with a spot diameter of 40 μm producing microtextured rough structure that provided high surface area for a variety of catalytic and electrocatalytic applications which will be explained further.

Microstructure morphology and feature size of the samples were further investigated using SEM images. SEM images of the pristine Cu and LIO-Cu surfaces with different magnifications are shown in Fig. 3. As observed in SEM images, the pristine Cu had a uniform surface with a dense metallic structure (Fig. 3a(i)). The high magnification images of the pristine Cu also showed smooth surface with some intrinsic structural defects and lamellar morphology (Fig. 3a(ii, iii)). Micrographs of four LIO-Cu samples prepared with different laser powers of 16, 24, 32, and 40 W are depicted respectively in Fig. 3(b–e). Low-magnification SEM images clearly showed a highly textured microstructure generated by laser beam on all LIO-Cu surfaces (Fig. 3b(i)–e(i)). While the 16LIO-Cu surface represents a randomly oriented microstructure (Fig. 3b(i)), raising the laser processing power to 24 W (Fig. 3c(i)) and 32 W (Fig. 3d(i)) led to the formation of more uniform microsphere structures of smaller sizes. Finally, by elevating the laser power to 40 W, a larger quantity of small spherical particles was formed. The average diameter of generated spheres on 40LIO-Cu sample was about $1.23 \pm 0.33$ μm (Fig. 3e(i)). The feature size distribution curves of all samples measured by ImageJ software and their associated SEM images are provided in the ESI† (Fig. S3). Laser beam with optimized powers could

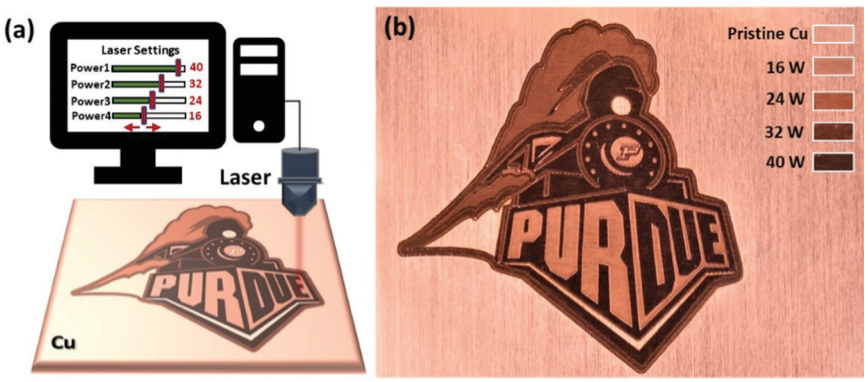


Fig. 1 (a) Schematic of the synthesis process of LIO-Cu with controlled laser power. (b) Realistic image of LIO-Cu patterned into Purdue University train logo using various laser powers.

 

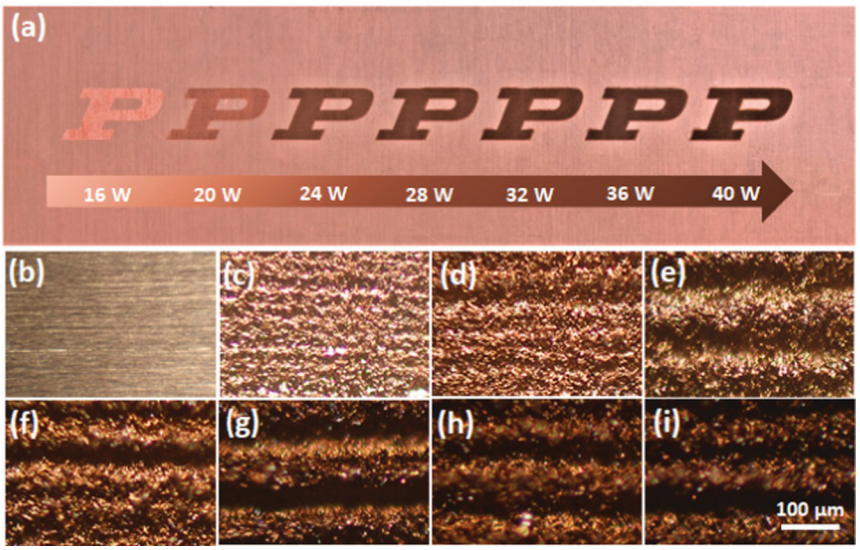


Fig. 2 (a) Purdue University logo ablated on copper surface using different laser powers. Optical microscopic images of (b) pristine copper and LIO-Cu surfaces fabricated using different laser powers of (c) 16 W, (d) 20 W, (e) 24 W, (f) 28 W, (g) 32 W, (h) 36 W, and (i) 40 W.

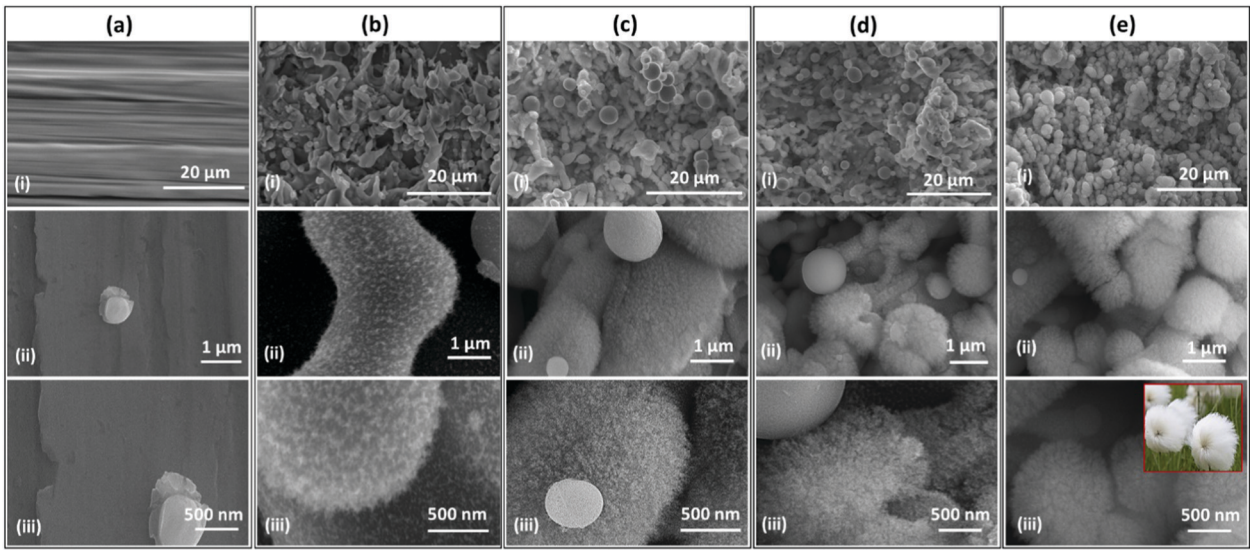


Fig. 3 SEM micrographs of (a) pristine copper and LIO-Cu surfaces fabricated using different laser powers of (b) 16 W, (c) 24 W, (d) 32 W, and (e) 40 W with (i) low, (ii) medium, and (iii) high magnifications. (e-iii) inset shows a realistic photo of cotton-grass for comparison.

induce growth of well-oriented copper oxide microspheres on copper surface with small size distribution. Laser power not only changed the microstructure of the LIO samples but also affected the final nanostructure on the textured microspheres which resulted in a unique hierarchical micro/nano scale combined copper oxide structure. In the 16LIO-Cu sample, some fine nanofeatures were visible at the surface of the microstructure (Fig. 3b(ii, iii)) which increased in quantity and ablation depth by raising the laser power to 24 W and 32 W (Fig. 3c(ii, iii), and d(ii, iii), respectively). The high magnification images of 40LIO-Cu sample showed a highly oriented cotton-grass like structure with nanowhiskers that covered the surface (Fig. 3e(ii, iii)). The inset in Fig. 3e(iii) represents a realistic image of a cotton-grass plant provided for structure comparison. The interaction of the high-power laser beam with copper surface accompanied by deep engraving of the surface *via* local heating, followed by a rapid cooling of the surface. This localized laser-induced sublimation of the copper surface resulted in formation of copper oxide nanoparticles that are subsequently self-organized and led to a hierarchical growth of the LIO-Cu structures on the surface as evidenced in the SEM images. At high laser power (*e.g.*, 40 W), laser beam provided high heat with greater ablation depth. Besides, the high temperature change between the heating step and subsequent rapid cooling of the surface caused an intense accumulation of the surface stress and grain refinement that

resulted in formation of finer microparticles.[51,52] The ablation profile and surface morphology are considered as a function of the spatial intensity distribution of the incident laser beam. Here we have utilized Nd:YAG laser with a common Gaussian beam profile. In general, during the laser interaction with the metal surface, a portion of the laser energy is absorbed into the material which leads to a parabolic profile of material ablation and thermal oxidation on the metal surface. Considering the narrow laser beam, laser processing areas greater than the size of the laser beam will require raster-scanning of the laser beam across the targeted surface in the form of parallel lines. Therefore, using different laser processing powers would not only results in different oxide compositions but also different levels of ablation depths into the metal substrate. The SEM images shown in Fig. S5(c and d) (ESI†) display an example of the rough microscale level parallel ablated lines that were generated on the 40LIO-Cu surface. Fig. S5(d) (ESI†) shows the overall surface profile of the laser processed metal samples that was generated by raster scanning of the laser beam with different powers while maintaining the constant line spacing ($\sim$100 μm). The surface of pristine-Cu sample was considered as reference level for all the profilometry measurements with average surface roughness of less than 0.5 μm. As predicted, the increase in laser processing power resulted in a relatively linear increase (370 nm $W^{-1}$) in the depths of the ablated region within the operating range of 16 W to 40 W. The maximum measured ablation depth was 10.8 $\pm$ 1.06 μm for 40LIO-Cu (prepared by the maximum laser power), Fig. S5(e) (ESI†). The change in the roughness and wettability of the copper surface was addressed using the SEM images of tilted samples and their water contact angle analysis that are shown in Fig. S6 (ESI†). Fig. S6-a and b (ESI†) evidently show the change in the surface features from pristine to LIO area. The enhanced roughness affected the wettability properties based on Wenzel theory,[53] which is demonstrated in Fig. S6-c (ESI†) (more information is provided in ESI†). The calculated values for water contact angle of the pristine-Cu, 16, 20, 24, 28, 32, 36, and 40 LIO-Cu samples were calculated as 95°, 63°, 40°, 31°, 18°, $<5°$, 0°, and 0°, respectively. The increased surface energy was caused by the decreased feature sizes and enhanced surface area of the LIO-Cu samples. Increased power showed enhanced laser texturing effect by providing a superhydrophilic surface for 36 and 40 LIO-Cu samples. Surface area and porosity data were obtained using $N_2$ adsorption–desorption technique. Brunauer–Emmett–Teller (BET) isotherm for $N_2$ adsorption–desorption analysis on 40LIO-Cu samples is shown in Fig. 4a. A type IV isotherm (based on IUPAC reports) with a H3 type hysteresis[54] representing presence of mesoporous structure was obtained and confirmed by the Barrett–Joyner–Halenda (BJH) pore size distribution data (Fig. 4b). The BJH data shows the pore sizes distributed between 4–10 nm representing mesoporous structure (typically 2–50 nm). BET analysis of 40LIO-Cu samples showed that the majority of the pores were within the range 5 nm with high effective surface area of 0.125 $m^2\ g^{-1}$.

EDX analysis of the samples were performed to determine the change in the composition by laser texturing. EDX plots for pristine and different LIO-Cu samples clearly revealed the increase in the oxygen level by increasing the laser power (Fig. 5a). Increased oxygen level referred to the oxidation of copper surface which was carried out by raising the temperature in the presence of atmospheric oxygen. Fig. 5b displays the ratio of oxygen in LIO-Cu samples compared to the oxygen in the pristine sample with respect to the change in laser power. As the laser power elevated, the oxygen ratio increased and finally at 40 W, the oxygen ratio enhanced significantly as compared to the pristine copper, representing high level of copper oxidation. The inset image in the Fig. 5b confirms this observation in EDX oxygen mapping of a sample depicting both pristine and LIO-Cu area. The two-sided area was further analysed for EDX line-scan which is shown in Fig. 5c. This plot demonstrated the enhanced oxygen level that is initiated from the boundary of the pristine copper and LIO-Cu area which has been affected by the generated heat at the joint LIO section.

The crystalline structures of the pristine copper and as-prepared LIO-Cu surfaces analysed by GI-XRD technique are presented in Fig. 6. XRD patterns for pristine copper and LIO-Cu samples in Fig. 6a exhibit intense peaks at 2$\theta$ values of

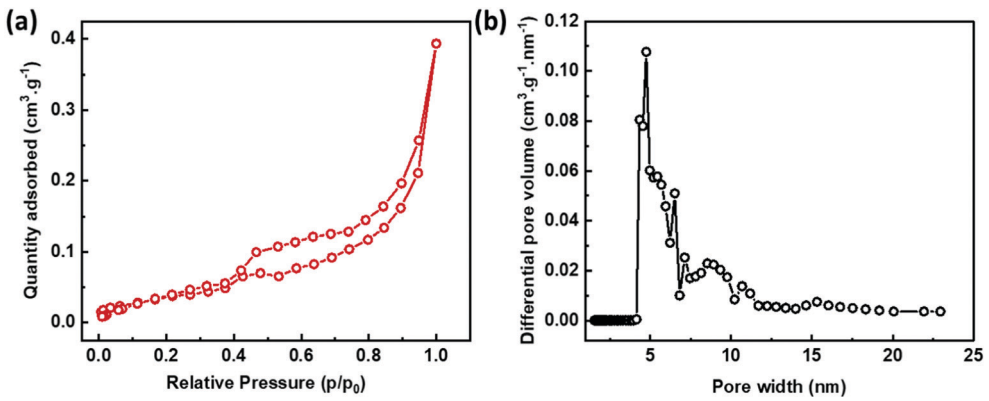


Fig. 4 (a) Nitrogen adsorption–desorption isotherm curves of pristine and 40LIO-Cu samples. (b) Barrett–Joyner–Halenda (BJH) plots showing pore-size distribution.

 

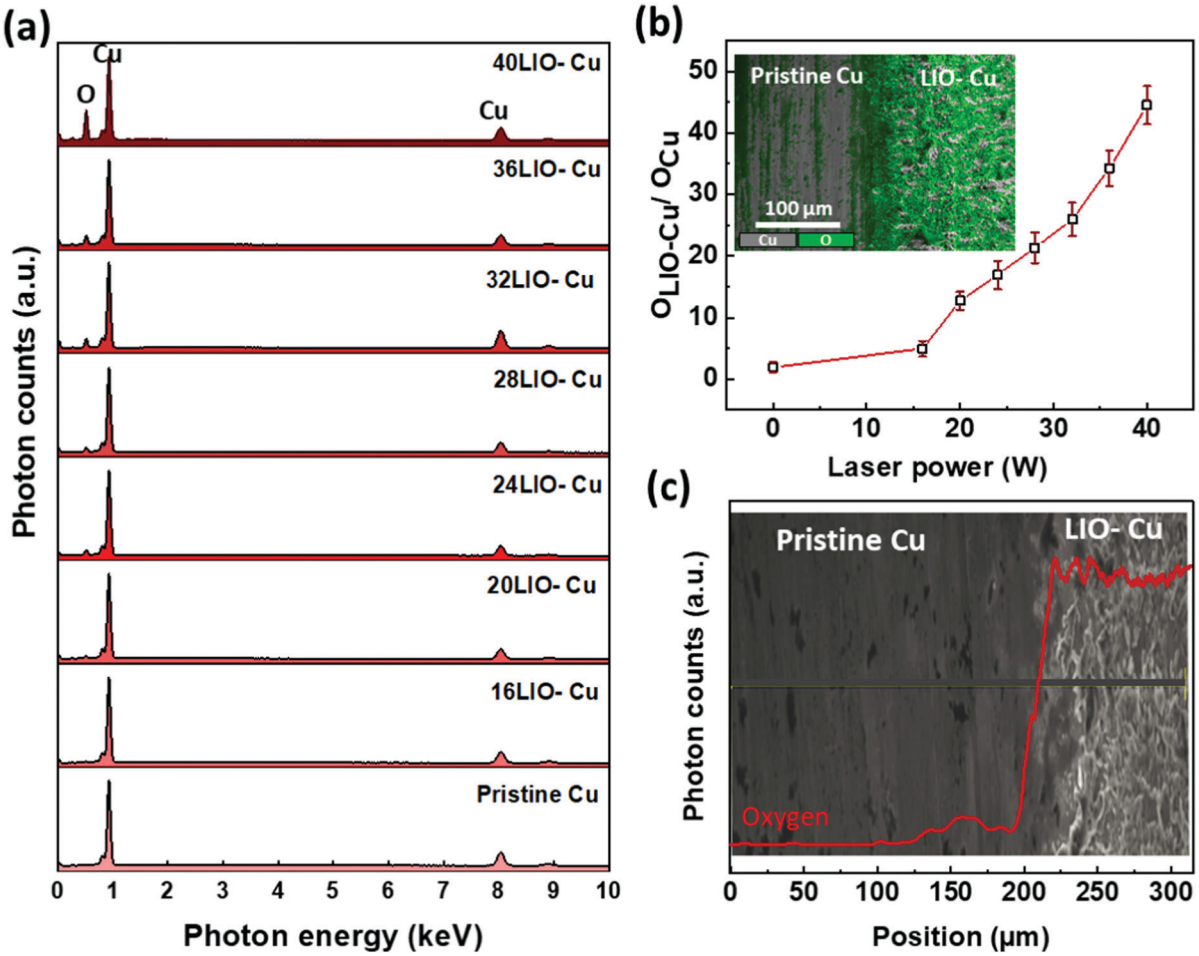


Fig. 5 (a) EDX plots for LIO-Cu samples. (b) Relative change in the level of oxygen by laser power; inset is EDX copper–oxygen map of 40LIO-Cu sample. (d) EDX line-scan for oxygen change on the 40LIO-Cu surface with associated sample in the background.

43.3°, 50.3°, and 73.4°, which are respectively indexed to the reflections from (111), (200), and (220) Cu planes with face-centered-cubic crystallinity (JCPDS 04-0836, and 01-085-1326).[55,56] In addition, the LIO-Cu samples showed a diffraction peak appeared at $2\theta = 36.47°$, which was attributed to the single-phase $Cu_2O$ (111) plane with a monoclinic structure (JCPDS 34-1354 and 01-078-2076).[56,57] This low-index crystalline facet made by a prompt LIO process, possesses excellent electrochemical and optical properties and can provide suitable sites for various catalytic, optical, and sensing applications.[22] Comparative XRD patterns plotted in Fig. 6b depicts the effect of laser power on the crystalline structure of LIO-Cu film. Fig. 6c illustrates the changes in the intensity of $Cu_2O$ (111) peak *versus* laser power. Increasing the laser power from 16 to 40 W led to a visible enhancement in the intensity of the $Cu_2O$ (111) peak. As it was mentioned earlier, the generated heat from laser beam could provide enough energy for the oxidation of Cu surface in the presence of the atmospheric oxygen. Besides, by increasing laser power, the increase in $Cu_2O$ content was intensified due to the decrease of feature sizes (as shown in SEM images in Fig. 3), which provided higher surface area to participate in the oxidation-reaction process with the atmospheric oxygen. A new $Cu_2O$ peak also appeared at high laser powers at $2\theta = 61.4°$, which can be assigned to the (311) plane (JCPDS 01-078-2076).[57] Although, the oxidation mechanism of copper is still yet to be completely understood, the factors such as temperature, oxygen level, and sample structures are found to play the main roles in this process. At ambient conditions, the ranges of preferential formation and coexistence of $Cu_2O$ and CuO phases are not completely known. However, reports showed that in atmospheric oxygen pressure, CuO was a stable phase, but by increasing the temperature (>1000 °C), $Cu_2O$ phase also became stable.[50] At high temperatures, the oxidation process of metals was known to be kinetically limited by the diffusion of species through the oxide layer. In this study, we overcame this limitation by a superficial oxidation process. Subsequently, creating fine particles through a fast melting and fusion at high laser powers could accelerate this process. Thus, a well-defined copper oxide layer was produced at the copper surface by a one-step, fast and reagent-less fabrication process.

Raman spectroscopy was carried out for further analysis of the as-prepared films in order to identify if other forms of copper oxides is present in the LIO-Cu samples. Raman spectra for the pristine copper and LIO-Cu samples are comparatively plotted in Fig. 7a. A distinctive enhancement in the Raman

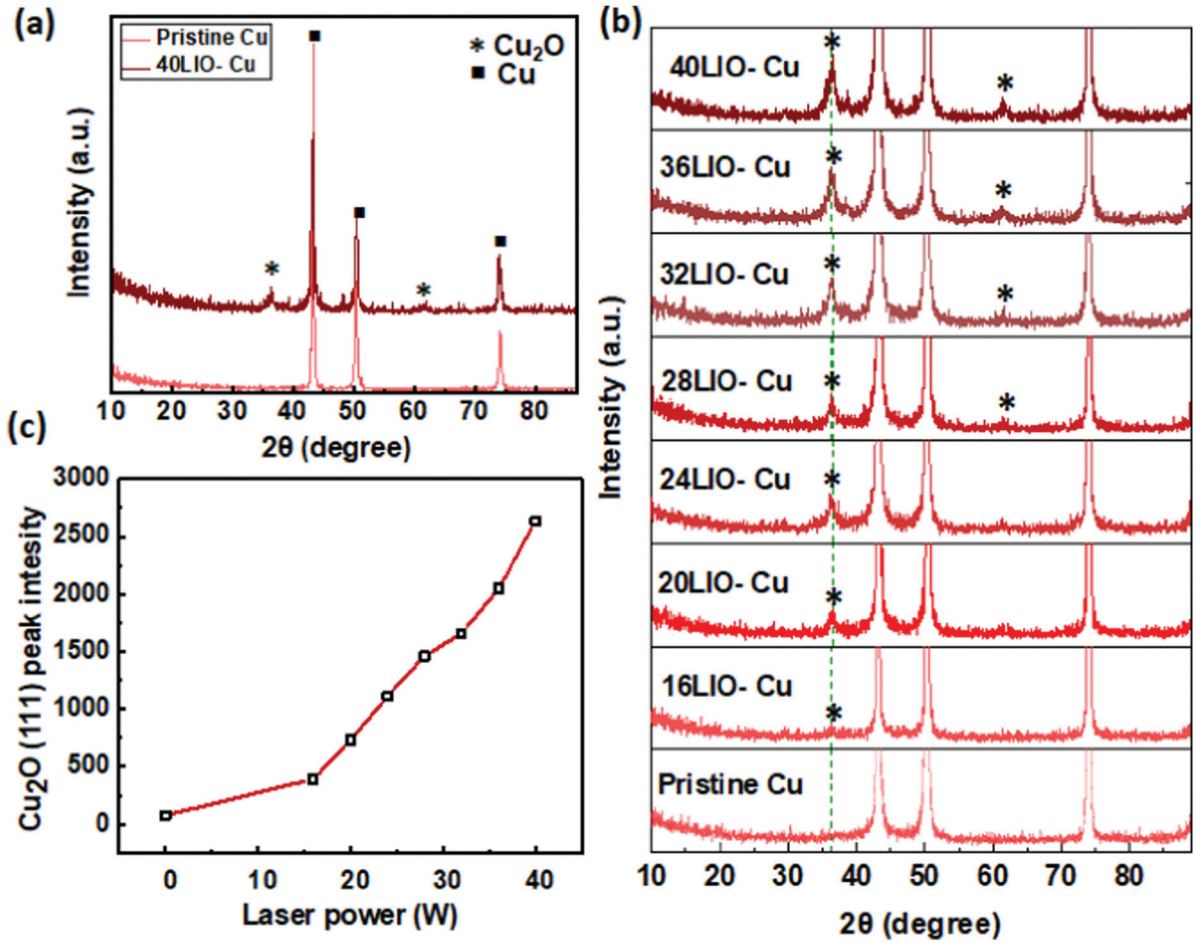


Fig. 6 (a) GI-XRD spectra for pristine and 40LIO-Cu sample. (b) Comparison of XRD spectra of pristine and different LIO-Cu samples tuned by laser power. (c) Change in (111) crystalline phase by changing laser power.

shifts by laser power were attributed to the change in the copper oxide level. The Raman shift at 638–665 $cm^{-1}$ corresponded to the out-of-phase motion of Cu and O in $Cu_2O$ sublattice, which is known as $T_{1U}$ symmetry mode.[50]

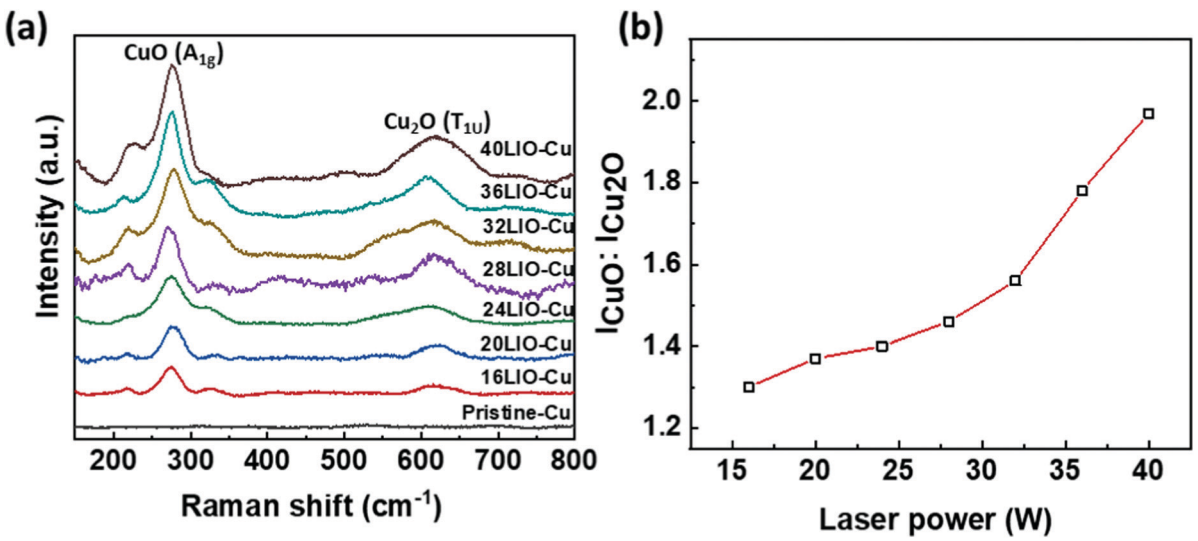


Fig. 7 (a) Raman spectra of LIO-Cu surfaces fabricated by different laser powers. (b) Change in the ratio of CuO to $Cu_2O$ Raman peak intensities by laser power.

 

Increase in this vibration mode confirmed the increase in the $Cu_2O$ sublattices, which was also evidenced by a crystalline structure shown in XRD analysis. Widening of this Raman shift by increasing the laser power can be explained by the decrease in the particle sizes which enhanced the Raman scattering. On the other hand, an intense Raman shift at about 296–300 $cm^{-1}$ was attributed to the Raman active vibration of $A_g$ symmetry in the CuO structure.[50] At high temperatures generated by the laser beam, the $Cu_2O$ species were prone to be further oxidized to form CuO. In conventional procedures, this oxidation process can be limited by the diffusion through the thick oxide layer. Here, the superficial oxidation process and fine structure of the top oxide layer provided an opportunity for further oxidation of $Cu_2O$ into CuO. Interestingly, CuO phase produced in this process did not exhibit any crystalline phase as evidenced in the XRD spectra, implying the possibility for the formation of an amorphous structure caused by a prompt oxidation of $Cu_2O$ on the outer copper surface. As both $Cu_2O$ and CuO phases tended to increase in quantity *via* increasing the laser power, controlled LIO process led to a controllable growth of $Cu_xO$ layer on the copper surface. Fig. 7b compares the changes in the ratio of CuO to $Cu_2O$ Raman peak intensities. While the total oxide level was increased by elevating the laser power, the ratio of $CuO:Cu_2O$ appeared to increase. The peak corresponding to the CuO species exhibited a higher enhancement compared to that of $Cu_2O$. In the initial stages of the oxidation process, the formation of $Cu_2O$ took place as a result of the oxidation of copper. As the $Cu_2O$ layer was formed by the LIO process, the particles on the upper part of the surface were subjected to further oxidation leading to the formation of CuO on the surface.[47] Absence of crystalline CuO peaks in the XRD spectra can be explained by a preferable formation of amorphous CuO phase on the copper surface through a prompt oxidation and re-organization process at the high laser power. However, amorphous phase of CuO is also reported to have high surface area exhibiting excellent electrochemical performance.[58,59] Besides, ATR-FTIR spectra of the sample surfaces revealed the peaks at about 980 $cm^{-1}$ and 1370 $cm^{-1}$ for Cu–OH vibration of orthorhombic phase of $Cu(OH)_2$ in LIO-Cu samples, and an IR peak observed at about 1550 $cm^{-1}$ which is associated with the Cu–O vibration of CuO[60] (Fig. S4, ESI†). The intensified Cu–O and Cu–OH vibrations by increasing the laser power is in good agreement with the XRD and Raman analysis data which demonstrated an increase in the $Cu_xO$ compounds by laser power.

## Electrochemical study

**Cyclic voltammetry.** Cyclic voltammetry data plotted in Fig. 8a demonstrates the oxidation and reduction peaks on a small 2 × 2 $mm^2$ area of the pristine and LIO-Cu samples in NaOH solution. As expected, the total current values in the applied potential range (−0.8 to +0.8 V) were significantly higher for the LIO samples as compared to the pristine Cu. This behaviour was caused by the presence of high levels of electrochemically active species on the surface of LIO samples. Anodic peaks at the applied potential values close to −0.4, −0.1, and +0.6 V were attributed to the oxidation of Cu, $Cu_2O$ and CuO species, respectively. While the oxidation peak of $Cu^0$ remained approximately the same, the oxidation peaks of Cu(I) and Cu(II) were significantly enhanced. Increased anodic peak intensities by increasing the laser powers verified electrochemically active behaviour of the low-index $Cu_2O$ (111) and amorphous CuO produced by LIO technique. Fig. 8b compares changes in the cathodic and anodic current *versus* laser power for one reduction and two oxidation potentials, respectively. The consistent gradual current enhancement by increasing the laser power showed the capability of this process for controllable fabrication of electrochemically active species.

These electrochemically active species were promising structures for non-enzymatic glucose oxidation. The CV analysis in the presence of 1 mM glucose solution demonstrated the glucose

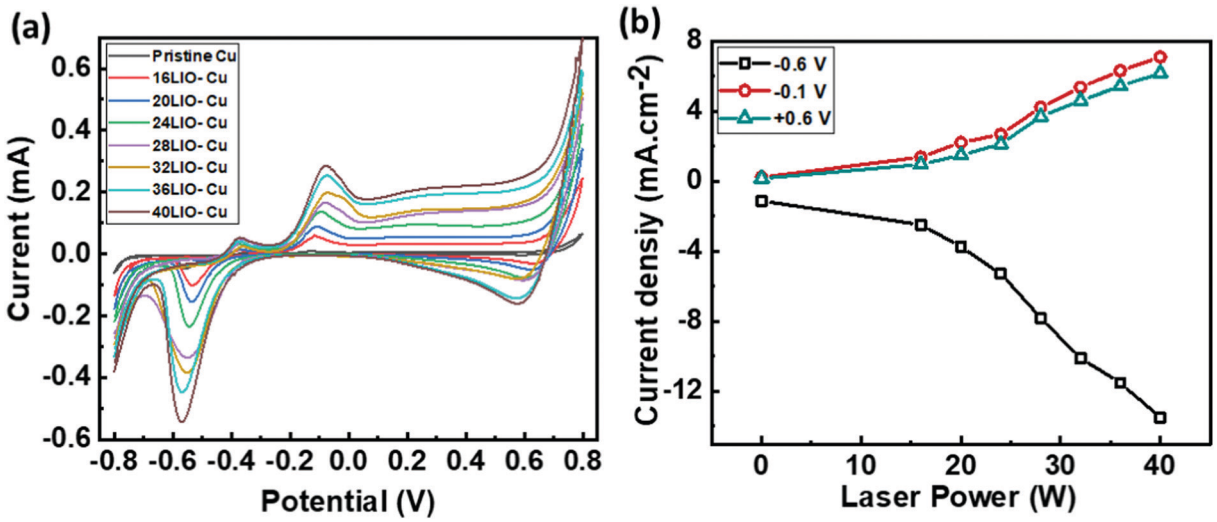


Fig. 8 Effect of laser power on electrochemical behaviour of LIO-Cu samples. (a) CV curves in 0.1 M NaOH (−0.8, 0.8 V) Scan rate: 50 mV $s^{-1}$ for different LIO-Cu samples. (b) Change in main CV oxidation and reduction current density at about −0.6, −0.1, and +0.6 V, by laser power applied for fabrication of LIO-Cu electrodes.

oxidation at about +0.6 V (Fig. 9a). The highest oxidation peaks belonged to the 40LIO-Cu sample which possessed the highest $CuO:Cu_2O$ ratio, based on the characterization data. Electrocatalytic oxidation of the glucose on copper-oxide-based electrodes in an aqueous media was carried out through oxidation of the aldehyde functional group to a carboxylic acid group (eqn (1)–(3));[28,61]

$$CuO + OH^- \rightarrow CuOOH + e^- \quad (1)$$

$$Cu(III) + \text{glucose} \rightarrow \text{Gluconolactone} + Cu(II) \quad (2)$$

$$\text{Gluconolactone} \rightarrow \text{Gluconic acid} \quad (3)$$

By applying oxidation potential, the Cu(II) and Cu(III) redox couple, drive the electrocatalytic glucose oxidation reaction in an aqueous solution. Upon addition of glucose content to the background solution, glucose molecule is being deprotonated. After deprotonation of glucose, the produced enediol form is being adsorbed onto the electrocatalyst surface (Cu(II) and Cu(III) surfaces) and oxidizes to gluconic acid.[55] The glucose oxidation mechanism on LIO-Cu surface is schematically illustrated in Fig. S7 (ESI†). This oxidation was represented as an increased current density of the anodic peak at about +0.6 V accompanied with the transformation of Cu(II) to Cu(III). By comparison of the current response of different LIO-Cu samples, 40LIO-Cu was selected as the optimized glucose sensor. Further studies were performed by comparing this electrode with the pristine-Cu sample. Fig. 9b and c are showing the CVs of pristine and 40LIO-Cu electrodes in different glucose concentrations ranging from 0 to 1 mM, respectively. Evidently, the current change by increasing the glucose content was remarkably higher for 40LIO-Cu than that of the pristine-Cu. The linear current change by glucose concentration is comparatively plotted in the Fig. 9d which indicates a notable difference in the slope for the 40LIO and pristine Cu electrodes which was due to the high quantity of electroactive components ($Cu_2O$ and CuO) and sufficient surface area for electrocatalytic reaction created by the laser texturing. It should be noted that not only higher laser power resulted in higher copper oxide compounds and greater glucose sensitivity performance, but also they resulted in deeper ablation depths into the metal substrate. For instance, 40LIO-Cu samples

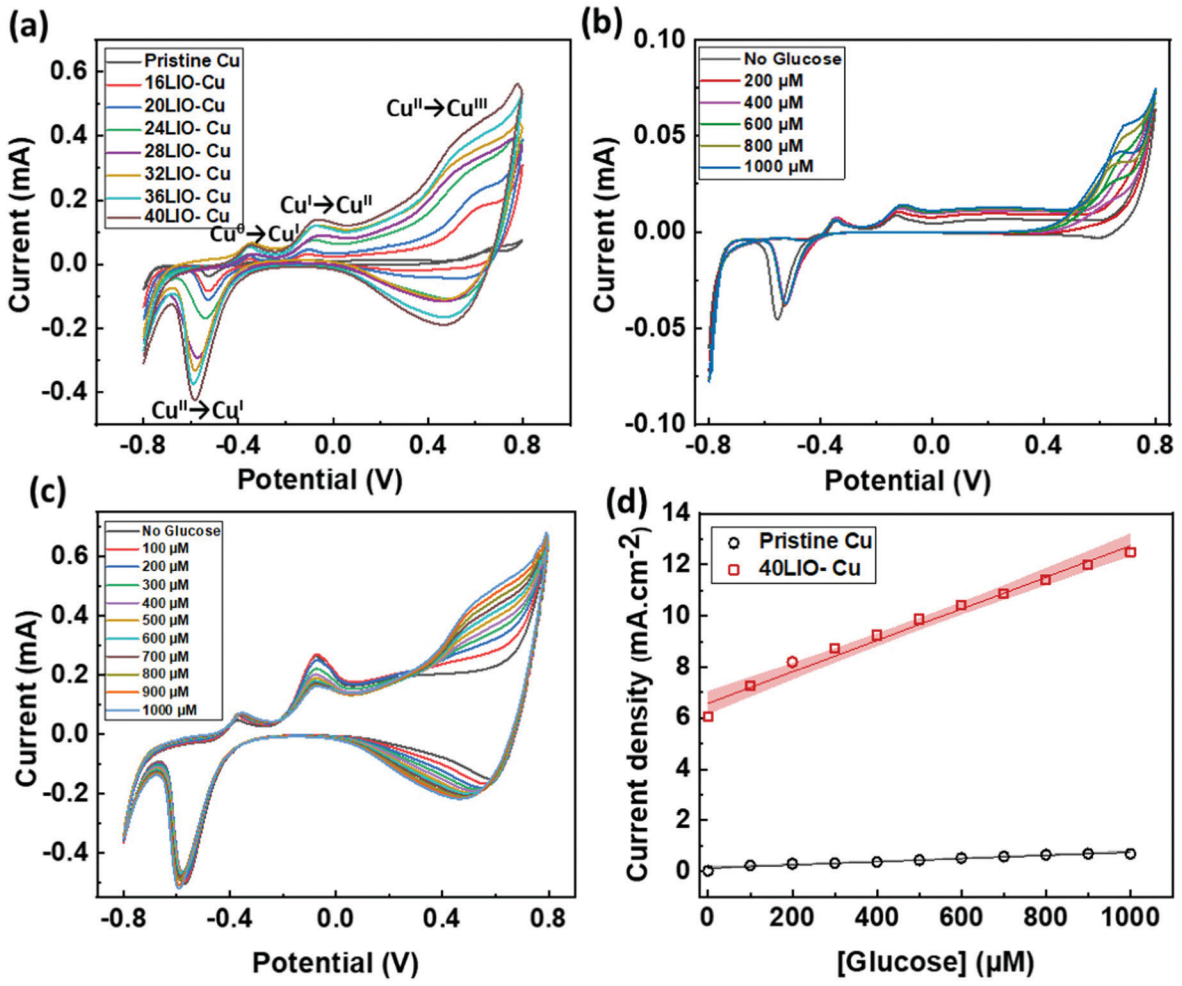


Fig. 9 CV curves for (a) different LIO-Cu samples in 1 mM glucose solution, (b) pristine-Cu and (c) 40LIO-Cu in different glucose concentrations; scan rate: 50 mV $s^{-1}$. (d) Comparison of current density change *versus* glucose concentration at about +0.6 V for pristine Cu and 40LIO-Cu electrodes.

 

had ablated grooves up to 10 μm inside the copper surface (Fig. S5(e), ESI†). Therefore, there is a trade-off between the level of electrocatalytic activity for glucose sensing and depth of material that will be ablated from the copper surface.

### Amperometric study

Evaluation of the glucose oxidation and sensitivity of the as-prepared samples with a dimension of 2 × 2 $mm^2$ was carried out using amperometric analysis by successive increasing the glucose concentration in PBS solution in successive increments. Based on the CV data, four different oxidation potentials of +0.4, +0.5, +0.6, and +0.7 V were investigated. Among different applied potentials +0.6 V provided the highest current response to glucose and therefore was selected as the optimum glucose oxidation potential for LIO-Cu electrodes (Fig. S8, ESI†). Fig. 10a shows the chronoamperometry plot for pristine-Cu and 40LIO-Cu. While the produced current on pristine-Cu by successive addition of glucose to the PBS solution was too low, 40LIO-Cu electrode showed an obvious current change even for the glucose concentrations as low as 10 μM. This electrode showed an exceptional sensitivity for a wide range of glucose concentrations from 10 μM to 5 mM with no further treatment or washing steps between the tests. This performance along with the fast response of the 40LIO-Cu electrodes were originated from its high surface area and electrocatalytic activity caused by LIO technique. The current response of 40LIO-Cu electrode *versus* glucose concentration is shown in Fig. 10b which shows a linear behaviour with an $R^2$ = 0.995 suggesting this electrode as a reliable glucose sensor for a wide range of concentrations. The calculated slope was 0.00695 ± 0.0001 mA $\mu M^{-1}$ $cm^{-2}$ (which was equal to the sensitivity of 6950 μA $mM^{-1}$ $cm^{-2}$) for a 2 × 2 $mm^2$ electrode. The limit of detection (LOD) value was calculated as 2.81 μM using the following equation based on a signal-to-noise ratio of 3.[62]

$$\mathrm{LOD} = \frac{3S}{m} \quad (4)$$

where $S$ is the standard deviation calculated from the blank signals (PBS electrolyte without added glucose) and $m$ is the slope of obtained calibration plot (Fig. 10b).

### Interference, repeatability, and reusability of 40LIO-Cu electrode

Other studies including selectivity, reproducibility, and long-term response stability were performed on 40LIO-Cu electrode towards glucose detection presented in Fig. 11. Possible interference from different agents including UA, As, AA, AC, GA, CA, and NaCl were studied by addition of 100 μM of glucose (from 10 mM stock solution) to the background PBS followed by successive addition of 100 μM of each agent (from 10 mM stock solution) into the solution. As it is evident from the plot in Fig. 11a, this electrode demonstrated a negligible current change by addition of the interfering agents while its response to glucose remained stable in the presence of all these agents. Response reproducibility of the 40LIO-Cu electrode which was evaluated for 17 cycles of switching from pure PBS to a PBS with 250 μM glucose is shown in Fig. 11b. The data showed a fast recovery time (estimated to be $<3$ seconds) and an appropriate response reproducibility of the 40LIO-Cu sensor toward glucose detection. This data indicated that this sensor can be used for multiple cycles without cleaning after each measurement. Long-term stability of the 40LIO-Cu sensor was also studied by running amperometric test for a concentration range of 10 to 1000 μM glucose every week. As it is shown in the Fig. 11c, this electrode showed an incredible reusability in glucose sensing with a highly stable response. The recorded sensitivity after 50 days was 92.3% of the initial sensitivity arising from its binder-free nanotextured structure which prevented the instability through leaching of the active sites. Furthermore, comparison of GI-XRD spectra of the 40LIO-Cu electrode before and after glucose detection showed no significant change in the crystallographic structure on the LIO-Cu surface even after exposure to 5 mM glucose solution (Fig. 11d). This observation further

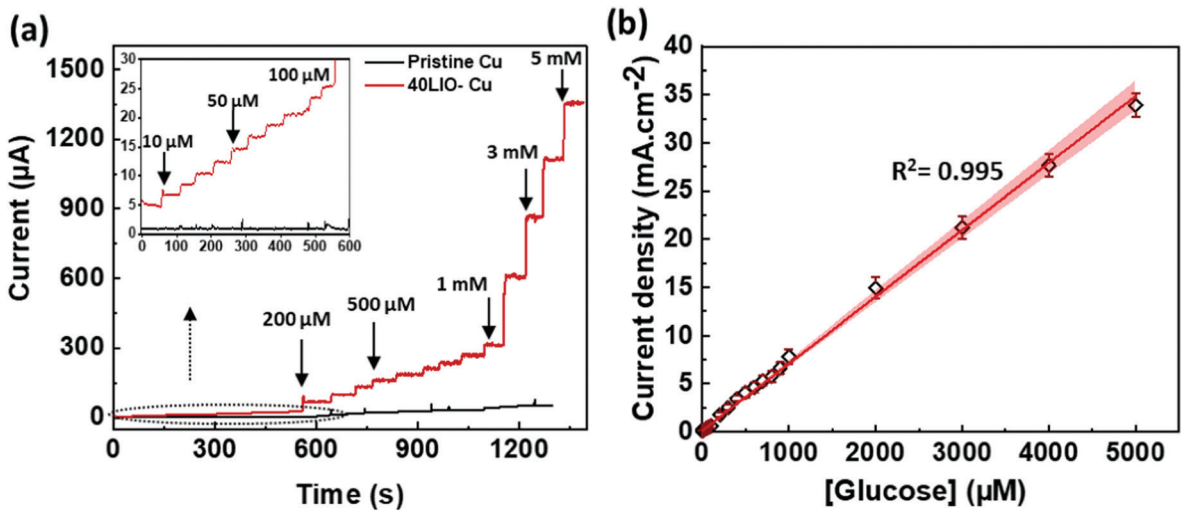


Fig. 10 Chronoamperometric response of LIO-Cu towards glucose. (a) Amperometric stepwise response of pristine copper and 40LIO-Cu electrode for successive addition of glucose to PBS buffer solution by applying +0.6 V potential. Change in current with glucose concentration.

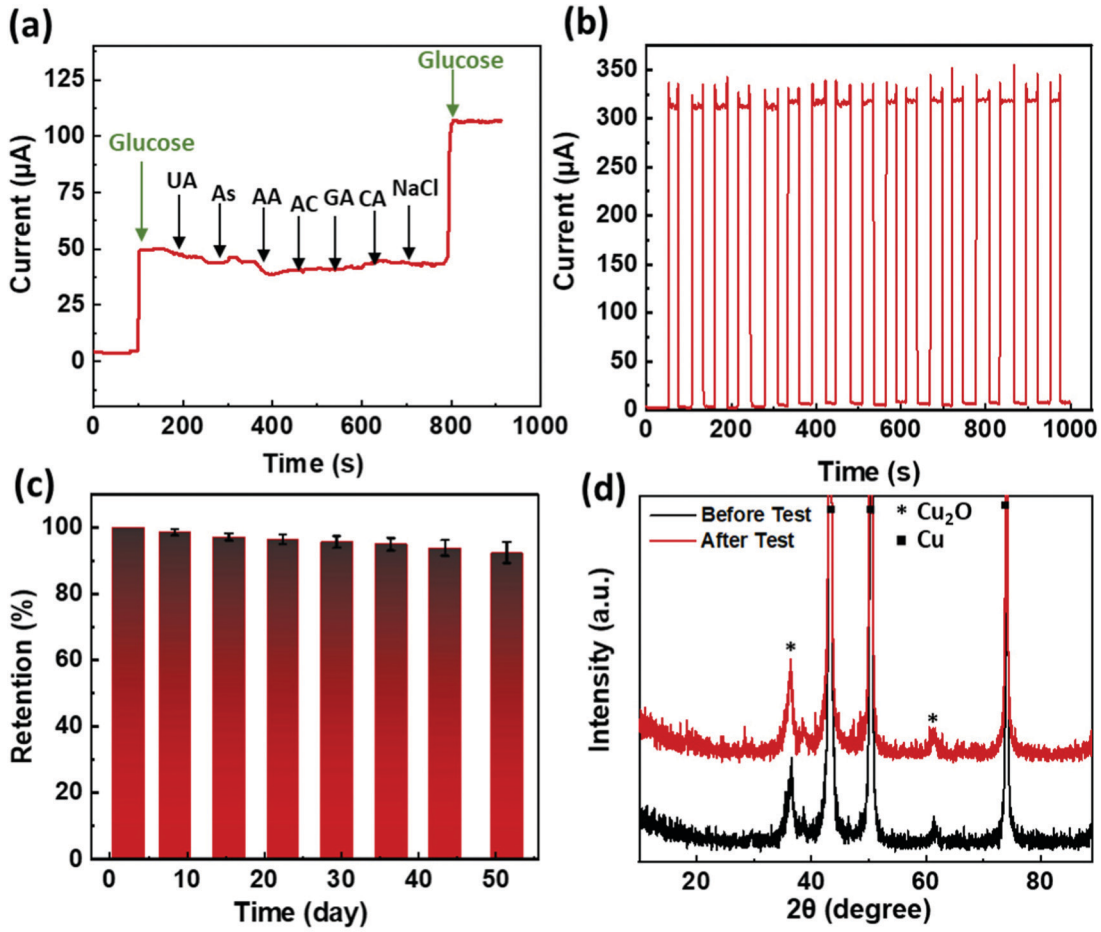


Fig. 11 Glucose detection performance of LIO-Cu electrode. (a) Selective response of the 40LIO-Cu electrode towards glucose in the presence of different interfering agents. (b) Response reproducibility of 40LIO-Cu electrode towards single concentration of glucose, 250 μM. (c) Long-term reusability of the 40LIO-Cu electrode for glucose detection in PBS buffer solution. (d) Comparison of XRD spectra for the LIO-Cu before and after glucose detection test in PBS (glucose concentrations of 5 mM).

confirmed the stability of copper oxide crystalline structure that was created on the LIO copper surface. Table 1 compares the performance of demonstrated LIO-Cu sensor in this work with some previously reported copper-based non-enzymatic glucose sensors. Despite the significantly lower fabrication complexity of our proposed LIO-Cu sensor, it represented an excellent glucose detection performance. Specifically, LIO-Cu sensor outperformed most of the newly developed Cu-based sensors in sensitivity and

Table 1 Comparison of sensing behaviour of our proposed LIO-Cu electrode with some of the Cu-based non-enzymatic glucose sensors. Measurements were performed using amperometric technique

| Sensor type | Preparation technique | Linear range (up to mM) | Sensitivity (μA $mM^{-1}$ $cm^{-2}$) | LOD (μM) | Working potential (V) | Long-term stability | Ref. |
|---|---|---|---|---|---|---|---|
| LIO-CuO/$Cu_2O$ | Laser induced oxidation | 5 | 6950 | 2.81 | +0.6 | 50 days (92.3%) | This work |
| NPG/CuO | Electrodeposition | 12 | 374 | 2.8 | +0.4 | N/A | 63 |
| $Cu_xO$/polypyrrole/Au | Electrodeposition | 8 | 232.22 | 6.2 | +0.6 | 10 days (96.2%) | 64 |
| CuO nanosheet/carbon cloth | Sputtering-wet etching | 1 | 4902 | 1 | +0.55 | 20 days (86.5%) | 65 |
| Cu(II)/MWCNT-COOH/GCE | Sonication and drop-casting | 9 | 2149 | 0.3 | +0.6 | N/A | 66 |
| Nano-coral arrays Cu | Electrodeposition | 5 | 1621 | 0.2 | +0.6 | 10 days (92.1%) | 67 |
| CuO NP/Pt | Inkjet printing | 6 | 1600 | 0.5 | +0.5 | N/A | 68 |
| Cu NP-LIG | Electroless deposition | 6 | 495 | 0.39 | +0.5 | 21 days (94.04%) | 69 |
| $Cu_xO$/Cu | Laser enhanced thermal oxidation | 1.6 | 1212.06 | 10 | +0.4 | N/A | 70 |
| Cu–PAni composite | Electrodeposition | 1 | 4140 | 5 | −0.45 | N/A | 71 |
| CuO hollow sphere | Hydrothermal | 16 | 35.2 | 1 | +0.55 | N/A | 72 |
| CuS/$Cu_2O$/CuO/Cu nanowire array | Anodization- annealing | 4 | 4262 | 2 | +0.6 | 21 days (92%) | 73 |
| 3D Cu foam- CuONWA | Wet-chemical method-annealing | 0.5 | 32 330 | 0.02 | +0.55 | 12 days (94.1%) | 74 |

 

long-term stability owing to its high surface area and binder-free nanostructure which provided robust electrocatalytic sites for glucose oxidation process.

## Conclusions

A high surface area nanotextured $CuO/Cu_2O$ layer was fabricated directly on top of a copper surface *via* a simple, fast, and low-cost LIO technique. Effects of laser power on structural properties, composition, crystallinity and oxide types and ratio were investigated using optical microscopy, FE-SEM, EDX, GI-XRD and Raman spectroscopy. Increased oxide level by increasing the laser power was confirmed and as-prepared samples were investigated for their electrochemical performance. The LIO-Cu samples demonstrated highly improved electrocatalytic activity arising from highly electroactive components of low-index crystalline $Cu_2O$ and amorphous CuO structure along with high surface area. The LIO-Cu electrodes were used as a non-enzymatic glucose oxidation electrocatalyst which showed ultra-high sensitivity. 40LIO-Cu as the optimized electrode was tested for sensitivity, selectivity, reproducibility, and long-term stability towards glucose detection. A fast detection with excellent sensitivity of 6950 $\mu A\ mM^{-1}\ cm^{-2}$ was recorded for a glucose concentration ranging from 10 μM to 5000 μM and LOD of 2.81 μM (S/N = 3). The as-prepared LIO-Cu sensor indicated a highly reproducible response for 17 successive measurement cycles with no cleaning process and a stable sensitivity for 50 days in ambient conditions.

## Author contributions

S. Sedaghat: conceptualization, methodology, material analysis, formal analysis, visualization, writing – original draft. S. Nejati: investigation, validation, material analysis, writing – review & editing. L. Regalado Bermejo: material analysis. Z. He: material analysis. A. M. Alcaraz: material analysis. A. Roth: validation. Z. Li: material analysis. V. G. Pol: resources, validation. H. Wang: resources, validation. R. Rahimi: conceptualization, funding acquisition, supervision, investigation, validation, project administration, writing – review & editing.

## Conflicts of interest

There are no conflicts to declare.

## Acknowledgements

The authors thank the staff of Purdue Birck Nanotechnology Center for their support. Funding for this project was provided by the Purdue University's Materials Engineering Department and SMART film Consortium at Birck Nanotechnology Center. S. S., S. N., L. R. B., and R. R. acknowledge the support from School of Material Engineering at Purdue University. We would like to acknowledge Guy Telesnicki for his assistance in cutting samples, Samuel Peana for his help on EDX-mapping, and Venkat Kasi for his precious inputs. Z. H. and H. W. acknowledge the support from the U.S. National Science Foundation (DMR-1809520) for the GIXRD effort.

## References

1 L. Wang, R. Zhang, T. Zhou, Z. Lou, J. Deng and T. Zhang, *Sens. Actuators, B*, 2017, **239**, 211–217.
2 J. Jang, S. Chung, H. Kang and V. Subramanian, *Thin Solid Films*, 2016, **600**, 157–161.
3 J. Han, J. Chang, R. Wei, X. Ning, J. Li, Z. Li, H. Guo and Y. Yang, *Int. J. Hydrogen Energy*, 2018, **43**, 13764–13777.
4 T. Jiang, M. Bujoli-Doeuff, E. Gautron, Y. Farré, L. Cario, Y. Pellegrin, M. Boujtita, F. Odobel and S. Jobic, *J. Alloys Compd.*, 2018, **769**, 605–610.
5 F. Li, Y. Li, J. Feng, Z. Gao, H. Lv, X. Ren and Q. Wei, *Biosens. Bioelectron.*, 2018, **100**, 512–518.
6 M. Liu, R. Liu and W. Chen, *Biosens. Bioelectron.*, 2013, **45**, 206–212.
7 D. Li, L. Meng, P. Xiao, D. Jiang, S. Dang and M. Chen, *J. Electroanal. Chem.*, 2017, **791**, 23–28.
8 T. K. Aparna, R. Sivasubramanian and M. A. Dar, *J. Alloys Compd.*, 2018, **741**, 1130–1141.
9 C. Espro, S. Marini, D. Giusi, C. Ampelli and G. Neri, *J. Electroanal. Chem.*, 2020, **873**, 114354.
10 N. Khaliq, M. A. Rasheed, G. Cha, M. Khan, S. Karim, P. Schmuki and G. Ali, *Sens. Actuators, B*, 2020, **302**, 127200.
11 M. Chen, Y. Wang, Y. Zhang, Y. Yuan, J. Liu, B. Liu, Q. Du, Y. Ren and H. Yang, *Sens. Actuators, B*, 2020, **310**, 127827.
12 O. Lupan, N. Ababii, A. K. Mishra, O. Gronenberg, A. Vahl, U. Schürmann, V. Duppel, H. Krüger, L. Chow, L. Kienle, F. Faupel, R. Adelung, N. H. de Leeuw and S. Hansen, *ACS Appl. Mater. Interfaces*, 2020, **12**, 42248–42263.
13 S. Deng, V. Tjoa, H. M. Fan, H. R. Tan, D. C. Sayle, M. Olivo, S. Mhaisalkar, J. Wei and C. H. Sow, *J. Am. Chem. Soc.*, 2012, **134**, 4905–4917.
14 S. John and S. C. Roy, *Appl. Surf. Sci.*, 2020, **509**, 144703.
15 T. Yang, Y. Ding, C. Li, N. Yin, X. Liu and P. Li, *J. Alloys Compd.*, 2017, **727**, 14–19.
16 H. Cheng, Q. Guan, L. F. Villalobos, K.-V. Peinemann, A. Pain and P.-Y. Hong, *Environ. Sci.: Nano*, 2019, **6**, 3467–3479.
17 S. Nejati, S. A. Mirbagheri, D. M. Warsinger and M. Fazeli, *J. Water Process Eng.*, 2019, **29**, 100782.
18 X. Jiang, W. Xu, W. Liu, M. Yue, Y. Zhu and M. Yang, *Fuel*, 2019, **241**, 777–785.
19 S. Anandan, J. J. Wu, D. Bahnemann, A. Emeline and M. Ashokkumar, *Colloids Surf., A*, 2017, **527**, 34–41.
20 A. A. Dubale, I. N. Ahmed, Y.-J. Zhang, X.-L. Yang and M.-H. Xie, *Appl. Surf. Sci.*, 2020, **534**, 147582.
21 X. Gao, J. Fei, Y. Shang and F. Fu, *Chin. J. Chem. Eng.*, 2018, **26**, 1508–1512.
22 Y. Shang and L. Guo, *Adv. Sci.*, 2015, **2**, 1500140.
23 S.-C. Hsu, S.-Y. Liu, H.-J. Wang and M. H. Huang, *Small*, 2015, **11**, 195–201.
24 S. Sedaghat, M. M. Ahadian, M. Jafarian and S. Hatamie, *Ind. Eng. Chem. Res.*, 2019, **58**(24), 10341–10351.

25 S. Sedaghat-Hoor and M. Anbia, *Part. Sci. Technol.*, 2019, **37**, 897–903.
26 S. Sedaghat, S. Jeong, A. Zareei, S. Peana, N. Glassmaker and R. Rahimi, *New J. Chem.*, 2019, **43**, 18619–18628.
27 C. S. Tan, S. C. Hsu, W. H. Ke, L. J. Chen and M. H. Huang, *Nano Lett.*, 2015, **15**, 2155–2160.
28 Y. Li, Y. Zhong, Y. Zhang, W. Weng and S. Li, *Sens. Actuators, B*, 2015, **206**, 735–743.
29 M. H. Huang, S. Rej and S.-C. Hsu, *Chem. Commun.*, 2014, **50**, 1634–1644.
30 X. Hong, G. Wang, W. Zhu, X. Shen and Y. Wang, *J. Phys. Chem. C*, 2009, **113**, 14172–14175.
31 Y. Yu, F.-P. Du, C. Y. Jimmy, Y.-Y. Zhuang and P.-K. Wong, *J. Solid State Chem.*, 2004, **177**, 4640–4647.
32 A. Henglein, *J. Phys. Chem. B*, 2000, **104**, 1206–1211.
33 T. Ikenoue, T. Kawai, R. Wakashima, M. Miyake and T. Hirato, *Appl. Phys. Express*, 2019, **12**, 055509.
34 X. Wang, M. Chen, Y. He and J. Zhu, *J. Alloys Compd.*, 2015, **628**, 50–56.
35 Z. Zhang, H. Che, J. Gao, Y. Wang, X. She, J. Sun, P. Gunawan, Z. Zhong and F. Su, *Catal. Sci. Technol.*, 2012, **2**, 1207–1212.
36 Y. Zhang, B. Deng, T. Zhang, D. Gao and A.-W. Xu, *J. Phys. Chem. C*, 2010, **114**, 5073–5079.
37 S. Sedaghat, C. R. Piepenburg, A. Zareei, Z. Qi, S. Peana, H. Wang and R. Rahimi, *ACS Appl. Nano Mater.*, 2020, **3**(6), 5260–5270.
38 V. Selvamani, A. Zareei, A. Elkashif, M. K. Maruthamuthu, S. Chittiboyina, D. Delisi, Z. Li, L. Cai, V. G. Pol and M. N. Seleem, *Adv. Mater. Interfaces*, 2020, **7**, 1901890.
39 R. Rahimi, M. Ochoa and B. Ziaie, *ACS Appl. Mater. Interfaces*, 2018, **10**, 36332–36341.
40 R. Rahimi, M. Ochoa, W. Yu and B. Ziaie, *ACS Appl. Mater. Interfaces*, 2015, **7**, 4463–4470.
41 S. Nejati, S. A. Mirbagheri, J. Waimin, M. E. Grubb, S. Peana, D. M. Warsinger and R. Rahimi, *J. Environ. Chem. Eng.*, 2020, 104109.
42 M. Ochoa, R. Rahimi and B. Ziaie, in *Stretchable Bioelectronics for Medical Devices and Systems*, Springer, 2016, pp. 207–226.
43 H. Jiang, M. Ochoa, R. Rahimi, W. Yu and B. Ziaie, *RSC Adv.*, 2019, **9**, 19531–19538.
44 H. J. Jung, Y. Yu and M. Y. Choi, *Bull. Korean Chem. Soc.*, 2015, **36**, 3–4.
45 L. Nánai, R. Vajtai and T. F. George, *Thin Solid Films*, 1997, **298**, 160–164.
46 A. Scandurra, F. Ruffino, S. Sanzaro and M. G. Grimaldi, *Sens. Actuators, B*, 2019, **301**, 127113.
47 L. B. Boinovich, K. A. Emelyanenko, A. G. Domantovsky, E. V. Chulkova, A. A. Shiryaev and A. M. Emelyanenko, *Adv. Mater. Interfaces*, 2018, **5**, 1801099.
48 G. Tang, A. C. Hourd and A. Abdolvand, *Appl. Phys. Lett.*, 2012, **101**, 231902.
49 J. F. Waimin, S. Nejati, H. Jiang, J. Qiu, J. Wang, M. S. Verma and R. Rahimi, *RSC Adv.*, 2020, **10**, 16313–16322.
50 D. Cakir, PhD thesis, Université Montpellier, 2017.
51 W. Stopyra, J. Kurzac, K. Gruber, T. Kurzynowski and E. Chlebus, Progress and Applications of Lasers, *Progress and Applications of Lasers*, International Society for Optics and Photonics, 2016, vol. 10159, p. 101590R.
52 I. N. M. Nawi, J. Ali, M. Fadhali and P. P. Yupapin, *Weld. Processes*, 2012, 75.
53 K. Kubiak, M. Wilson, T. Mathia and P. Carval, *Wear*, 2011, **271**, 523–528.
54 L. Nie, A. Meng, J. Yu and M. Jaroniec, *Sci. Rep.*, 2013, **3**, 1–6.
55 T. Theivasanthi and M. Alagar, 2011, aarXiv:1110.1372.
56 B. D. Du, D. T. B. Ngoc, N. D. Thang, L. N. A. Tuan, B. D. Thach and N. Q. Hien, *Vietnam J. Chem.*, 2019, **57**, 318–323.
57 M. Devaraj, R. Saravanan, R. Deivasigamani, V. K. Gupta, F. Gracia and S. Jayadevan, *J. Mol. Liq.*, 2016, **221**, 930–941.
58 V. Patake, S. Joshi, C. Lokhande and O.-S. Joo, *Mater. Chem. Phys.*, 2009, **114**, 6–9.
59 Z. Tian, H. Bai, Y. Li, W. Liu, J. Li, Q. Kong and G. Xi, *ChemistryOpen*, 2020, **9**, 80–86.
60 S. K. Shinde, D. P. Dubal, G. S. Ghodake, P. Gomez-Romero, S. Kim and V. J. Fulari, *RSC Adv.*, 2015, **5**, 30478–30484.
61 S. T. Farrell and C. B. Breslin, *Electrochim. Acta*, 2004, **49**, 4497–4503.
62 H. Singh, J. Bernabe, J. Chern and M. Nath, *J. Mater. Res.*, 2021, 1–12.
63 X. Xiao, H. Li, Y. Pan and P. Si, *Talanta*, 2014, **125**, 366–371.
64 F. Meng, W. Shi, Y. Sun, X. Zhu, G. Wu, C. Ruan, X. Liu and D. Ge, *Biosens. Bioelectron.*, 2013, **42**, 141–147.
65 Y. Zhong, T. Shi, Z. Liu, S. Cheng, Y. Huang, X. Tao, G. Liao and Z. Tang, *Sens. Actuators, B*, 2016, **236**, 326–333.
66 W. Zheng, Y. Li, L. Hu and L. Y. S. Lee, *Sens. Actuators, B*, 2019, **282**, 187–196.
67 H. Chen, G. Fan, J. Zhao, M. Qiu, P. Sun, Y. Fu, D. Han and G. Cui, *New J. Chem.*, 2019, **43**, 7806–7813.
68 R. Bernasconi, A. Mangogna and L. Magagnin, *J. Electrochem. Soc.*, 2018, **165**, B3176.
69 Y. Zhang, N. Li, Y. Xiang, D. Wang, P. Zhang, Y. Wang, S. Lu, R. Xu and J. Zhao, *Carbon*, 2020, **156**, 506–513.
70 S. Wang, L. Jiang, J. Hu, Q. Wang, S. Zhan and Y. Lu, *J. Alloys Compd.*, 2020, **815**, 152105.
71 O. Belgherbi, D. Chouder, D. Lakhdari, C. Dehchar, S. Laidoudi, L. Lamiri, A. Hamam and L. Seid, *J. Inorg. Organomet. Polym. Mater.*, 2020, 1–10.
72 Z. Haghparas, Z. Kordrostami, M. Sorouri, M. Rajabzadeh and R. Khalifeh, *Biotechnol. Bioprocess Eng.*, 2020, **25**, 528–535.
73 C. Wei, X. Zou, Q. Liu, S. Li, C. Kang and W. Xiang, *Electrochim. Acta*, 2020, **334**, 135630.
74 X. Liu, W. Yang, L. Chen and J. Jia, *Electrochim. Acta*, 2017, **235**, 519–526.

 